Brain Structure and Function (2019) 224:779–793
https://doi.org/10.1007/s00429-018-1806-y

ORIGINAL ARTICLE

Asymmetric effective connectivity between primate anterior cingulate and lateral prefrontal cortex revealed by electrical microstimulation

Verónica Nácher[1] · Seyed Alireza Hassani[1,2] · Thilo Womelsdorf[1,2]

Received: 21 May 2018 / Accepted: 27 November 2018 / Published online: 1 December 2018

Abstract

The dorsal anterior cingulate cortex (dACC) and lateral prefrontal cortex (lPFC) of the non-human primate show neural firing correlations and synchronize at theta and beta frequencies during the monitoring and shifting of attention. These functional interactions might be based on synaptic connectivity that is equally efficacious in both directions, but it might be that there are systematic asymmetries in connectivity consistent with reports of more effective inhibition within the dACC than lPFC, or with a preponderance of dACC projections synapsing onto inhibitory neurons in the lPFC. Here, we tested effective dACC-lPFC connectivity in awake monkeys and report systematic asymmetries in the temporal patterning and latencies of effective connectivity as measured using electrical microstimulation. We found that dACC stimulation-triggered evoked fields (EFPs) were more likely to be multiphasic in the lPFC than in the reverse direction, with a large proportion of connections showing 2–4 inflection points resembling resonance in the 20–30 Hz beta frequency range. Stimulation of dACC → lPFC resulted, on average, in shorter-latency EFPs than lPFC → dACC. Overall, latencies and connectivity strength varied more than twofold depending on the precise anterior-to-posterior location of the connections. These findings reveal systematic asymmetries in effective connectivity between dACC and lPFC in the awake non-human primate and document the spatial and temporal patchiness of effective synaptic connections. We discuss that our results suggest that measuring effective connectivity profiles will be essential for understanding how asymmetries in local synaptic efficacy and connectivity translate into functional neuronal interactions during adaptive, goal-directed behavior.

Keywords Anterior cingulate cortex · Lateral prefrontal cortex · Effective connectivity · Electrical stimulation · Cortical mapping · Monkey

Introduction

The anterior cingulate cortex and the lateral prefrontal cortex in primates are believed to exchange information during attention-demanding tasks and when following behavioral feedback (Alexander and Brown 2011; Shenhav et al. 2016; Rushworth et al. 2011). This information exchange is essential for successful attentional deployment and for adjusting behavioral strategies (Womelsdorf and Everling 2015; Hayden et al. 2011; Kennerley et al. 2006). Functionally, this information exchange becomes evident in activity correlations during attention shifts and outcome processing in the form of bilateral dACC-lPFC firing correlations (Oemisch et al. 2015), spike-burst to local field potential (LFP) synchronization in the theta, beta, and gamma band (Womelsdorf et al. 2014a, b), burst-triggered LFP power correlations at theta and beta frequencies (Voloh and Womelsdorf 2017), inter-areal theta-phase-to-gamma-amplitude correlations (Voloh et al. 2015), and beta and gamma band LFP correlations (Rothe et al. 2011). The synaptic- and circuit-level mechanisms that underlie this heterogeneous pattern of functional correlations are largely unknown. One reason for this knowledge gap is the unknown efficacy of neuronal connections between both brain areas that could indicate how strong, fast, symmetric, and frequency-specific neuronal interactions are between both areas. Our study set

✉ Verónica Nácher
vnacherc@yorku.ca

✉ Thilo Womelsdorf
thilo.womelsdorf@vanderbilt.edu

[1] Centre for Vision Research, York University, 4700 Keele Street, Toronto, ON M3J 1P3, Canada

[2] Department of Psychology, Vanderbilt University, PMB 407817, 2301 Vanderbilt Place, Nashville, TN 37240-7817, USA

out to provide this missing link in understanding the interplay of circuits in dACC and lPFC in the awake rhesus monkey.

Previous anatomical studies have shown bidirectional synaptic connectivity between dACC and lPFC (Arikuni et al. 1994; Lu et al. 1994; Morecraft et al. 2012). This bidirectional connectivity might reveal systematic anatomical asymmetries whose functional consequences are poorly understood (Barbas 2015). For example, quantitative studies have shown more numerous populations of parvalbumin expressing (PV+) inhibitory interneurons in lPFC than in dACC, but larger densities of slower acting calbindin (CB+) expressing interneurons in dACC than lPFC (Dombrowski et al. 2001). These neuron-specific differences are likely paralleled by pathway specific differences in the size of boutons and spines (Medalla and Barbas 2010; Medalla et al. 2017), and in different number of cells that are within the synaptic terminal fields of dACC → lPFC versus lPFC → dACC connections (Gabbott and Bacon 1996; Medalla et al. 2017). From a functional perspective, these anatomical anisotropies are expected to be reflected in unique efficacy profiles, and possibly in a unique temporal patterning of neuronal interactions between both areas. However, it is difficult to constrain hypotheses about the precise consequences of specific structural connectivity differences for functional interactions without some ground truth about the efficacy of inter-areal connections.

Our study, therefore, set out to identify the electrical microstimulation parameter range that allows characterizing the strength, timing, temporal patterning and anatomical specificity of dACC → lPFC, and lPFC → dACC connectivity in the awake non-human primate. We found that stimulation-evoked fields showed a similar amplitude dependence and multiphasic patterning in both stimulation directions. Beyond these similarities, we revealed prominent differences with shorter lPFC → dACC latencies, and slower temporal beta frequency range resonance following lPFC → dACC stimulation compared to dACC → lPFC stimulation. We believe that these insights provide constraints to understand how structural connections and circuit compositions lead to unique profiles of functional interactions.

Materials and methods

Subjects and surgical procedures

Experiments were conducted in two adult male monkeys (*Macaca Mulatta*) weighing 11 kg (Monkey S) and 8 kg (Monkey H). Both were implanted with a head holder for immobilizing the head during experiments and with a rectangular recording chamber (20 × 28 mm inner dimensions), placed over the right hemisphere, above the lPFC and dACC following stereotaxic coordinates (Paxinos et al. 2008) and magnetic resonance imaging (MRI). All surgical procedures were carried out under general anesthesia and aseptic conditions. The animals were first anesthetized with ketamine (10 mg/kg i.m.), acepromazine (0.5 mg/kg, i.m.) and atropine (0.04 mg/kg, i.m.), followed by isoflurane anesthetic until a surgical level of anesthesia was achieved. Animals were intubated and artificially ventilated with a mixture of oxygen and air. Expiratory CO2, electrocardiogram trace and temperature were monitored continuously during surgery. Antibiotics and analgesics were administered after surgery. All procedures followed the guidelines of the Canadian Council of Animal Care policy on the use of laboratory animals and were approved by the Council on Animal Care of York University.

Electrical stimulation and recording sessions

During the experiments, the monkeys sat in a custom-made primate chair with their head stabilized and were kept alert but quiet by receiving drops of juice after each stimulation protocol (controlled by the experimenter). We either stimulated lPFC and recorded single neurons and local field potentials (LFPs) in dACC or vice versa using tungsten microelectrodes (FHC). The stimulation microelectrodes were 250 µm in diameter with an impedance of 0.1 MΩ and the recording microelectrodes were 125 µm in diameter with an impedance of 1.2–2.2 MΩ. Microelectrodes were lowered daily through guide tubes using software-controlled precision microdrives (Neuronitek, ON, Canada). We typically placed two stimulating microelectrodes in one microdrive, using separate adjacent guide tubes mounted to the microdrive (interelectrode distance of 1 mm), for wide bipolar stimulation (Montgomery 2010). Two recording microelectrodes were placed in a second microdrive in the same manner. The two microdrives were mounted on the recording chamber and the distance between them during the experiment was 6 mm on average. Stimulating and recording microelectrodes in both regions were always at the same interaural level (Fig. 1a). The recorded or stimulated subfields in lPFC (areas 9/46, 46d, 46v) and dACC (areas 32, 24c) (Fig. 1a) were identified by projecting each electrode trajectory onto the two-dimensional brain slices obtained from anatomical MRI images, using the open-source MRIcro imaging software (http://www.mricro.com). At the beginning of each experiment, all microelectrodes were connected to a multichannel acquisition processor (Neuralynx Digital Lynx system, Inc., Bozeman, Montana, USA) for data amplification, filtering, and acquisition. Spiking activity was obtained following a 600–8000 Hz bandpass filter and further amplification and digitization at a 32 KHz sampling rate. LFP signals were obtained by low-pass filtering at 300 Hz and downsampling to 1 KHz. Microelectrodes in both microdrives were

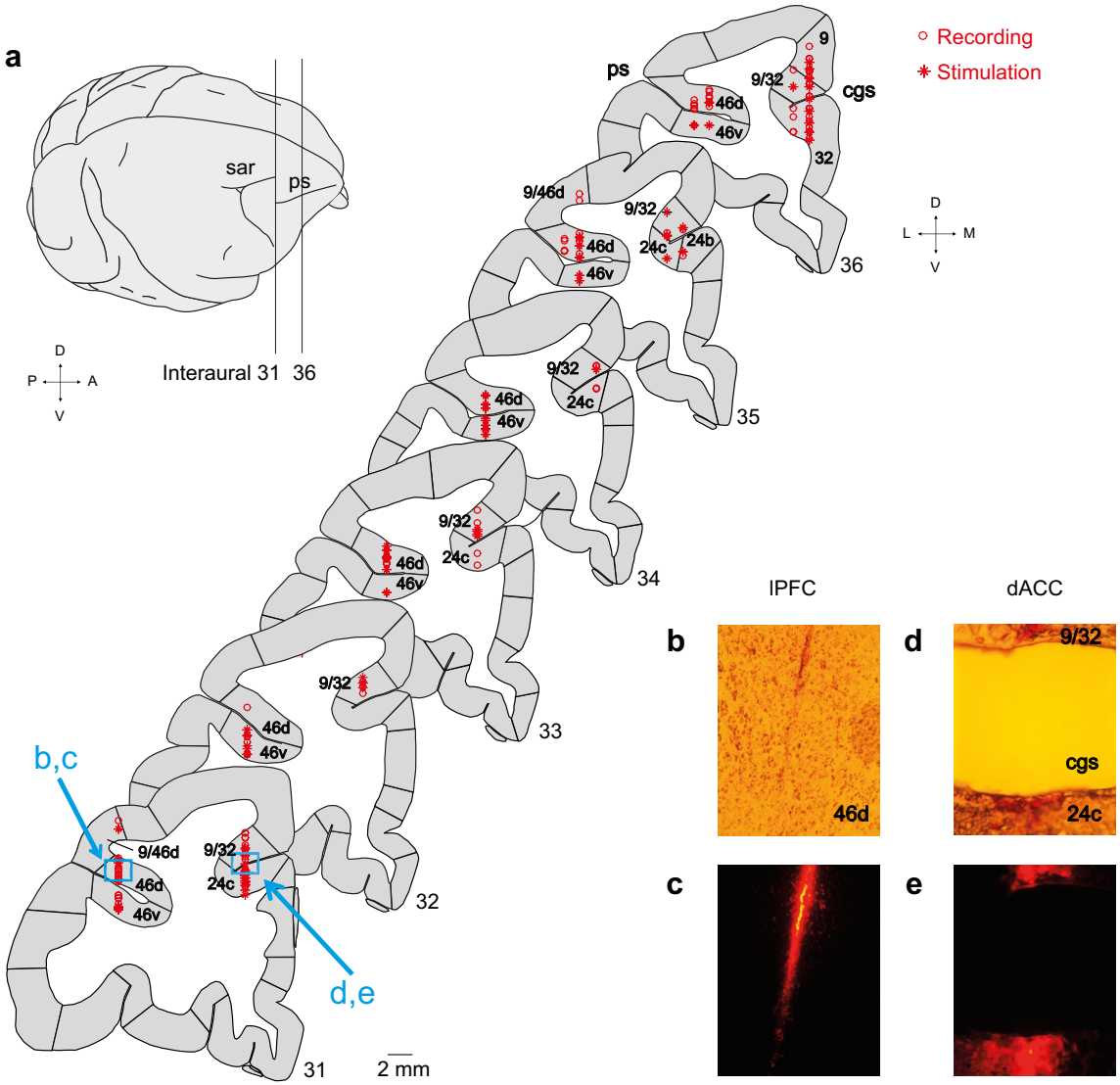

Fig. 1 Anatomical reconstruction of the stimulation (open circles) and recording sites (asterisks) in dACC and lPFC areas. **a** Right lateral surface of the rhesus monkey brain. The vertical lines depict the limits of the location of six plates in the coronal plane shown on the right. In each coronal plate the number at the bottom right shows the anterior–posterior distance relative to the interaural line (Paxinos et al. 2008). **b, d** Bright-field micrograph of regions indicated in **a** (blue squares) for lPFC area 46d (**b**) and dACC areas 9/32 and 24c (**d**). **c, e** Fluorescent photomicrographs of the same fields and sections in **b** and **d** showing the dye traces left by microelectrodes. The punctuated areas of high fluorescence are cell bodies that have incorporated the dye (DiI). Abbreviations: sar, superior arcuate sulcus; ps, principal sulcus; cgs, cingulate sulcus; lPFC, lateral prefrontal cortex; dACC, anterior cingulate cortex. Axes: *D* dorsal, *V* ventral, *A* anterior, *P* posterior, *L* lateral, *M* medial

advanced into the brain at the calculated coordinates for the specific lPFC and dACC subfields and until spiking activity was recorded, for making sure that the stimulation microelectrodes were located in gray matter. Bipolar electrical microstimulation proceeded using the StimPulse Electrical Stimulator System (FHC). Constant currents were delivered to the stimulating microelectrodes and consisted of a single pulse or bursts of 2, 4 or 8 pulses each (Fig. 2a). Each pulse was biphasic, rectangular, and charge-balanced (190 µs width for each phase with 10 µs pulse delay) with the cathodal pulse preceding the anodal. The inter-pulse delay for burst stimulation was 2 ms. During initial experiments, a range of intensities between 20 and 240 µA with increasing steps of 20 µA, and a range of 300–1000 µA with increasing steps of 100 µA was tested in the first animal. However, we subsequently determined that stimulation intensities of 40, 140, 240, and 500 µA provided a good range for activating the circuits which were then selected for the experimental mapping of effective connectivity in both monkeys (Fig. 2b). During a typical stimulation protocol, single pulses or

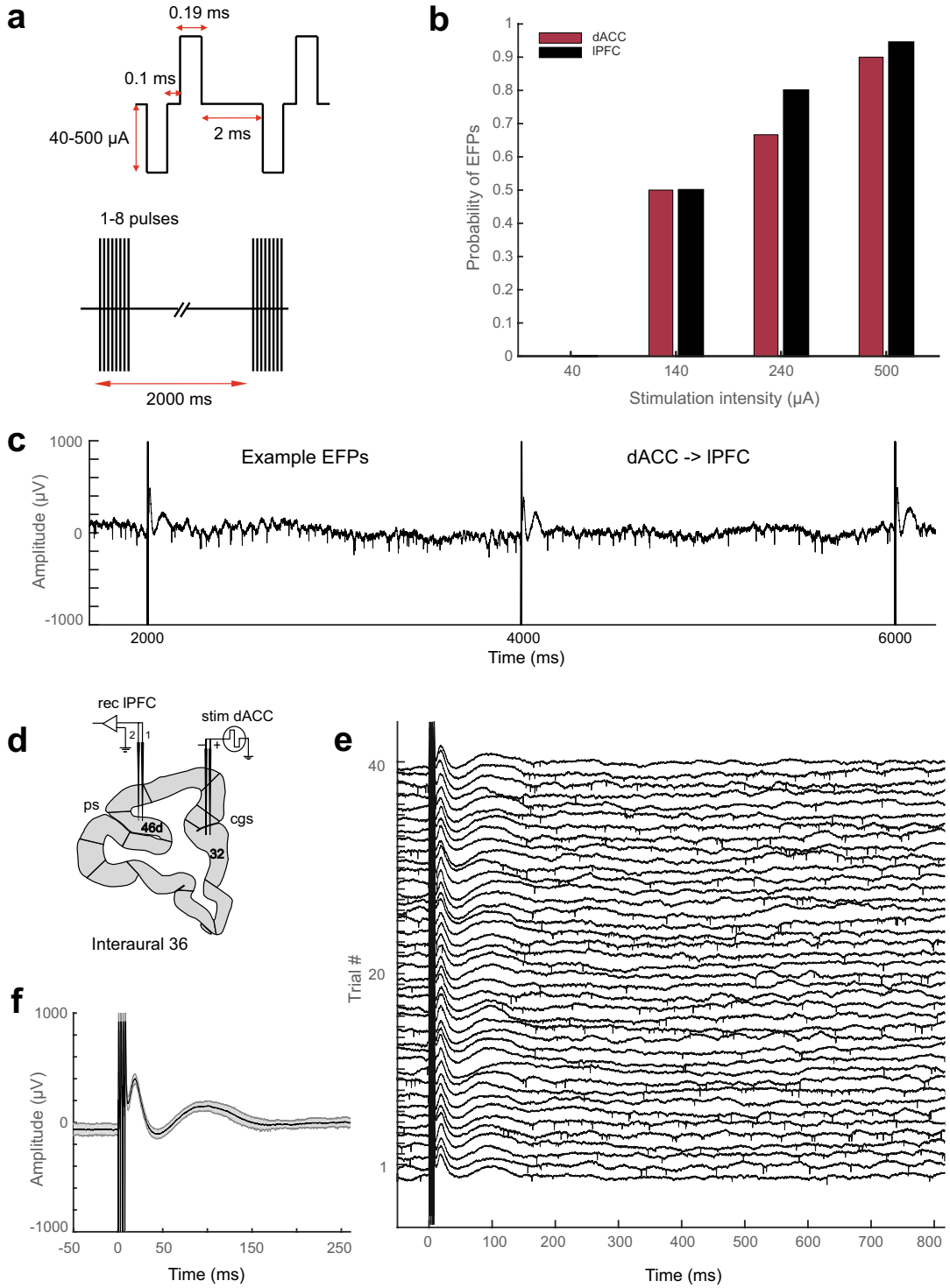

Fig. 2 Example procedures for stimulating and recording evoked field potentials (EFPs). **a** Parameters of the biphasic pulses used for stimulation. **b** Probability of eliciting long-distance EFPs across sites. Each bar represents the probability of causing an EFP as function of the stimulation amplitude. Following single pulse stimulation, the least stimulation intensity which produced an EFP in 50% of the recording sites in dACC and lPFC areas is 140 µA. **c** Example wideband lPFC recording (LFP and spikes) showing the stimulation timing during three example-stimulating bursts of four pulses each (vertical lines). EFPs can be seen following each burst. **d** Experimental setup for dACC stimulation and lPFC recording with which the example EFPs were obtained. **e** Same description as in **c**, but showing the EFPs for all 40 trials. Reliable and consistently activated EFPs follow each stimulation burst. **g** Average EFPs in lPFC following 40 stimulation bursts. Shaded error bars represent the variability of the averaged EFPs over 40 trials (mean ± SEM)

bursts were repeated every 2 s for a total number of 40 trials (Fig. 2a). We used microstimulation to determine whether dACC and lPFC show effective connectivity. In half of the sessions, dACC neurons were stimulated and activation of the lPFC was recorded. If the recorded lPFC sites received input from dACC, then an evoked field potential (EFP) could be reliably observed for each dACC stimulation trial (e.g., Fig. 2c, d). In the other half of the sessions, we tested the directionality of the circuit by stimulating lPFC and recording from dACC in either the same or similar locations used for stimulation and recording in the preceding sessions. The depths of the stimulation and recording microelectrodes were adjusted under electrophysiological monitoring of the LFPs until EFPs were triggered. Data collection started 5 s before stimulation (pre-stimulation period) and continued for 5 s after stimulation (post-stimulation period). The 40 stimulations at the same stimulation and recording depths and locations were averaged for later analysis (Fig. 2e, f).

Data analysis

Responses were analyzed offline using matlab (The Mathworks, Inc.). The majority of EFPs recorded in dACC and lPFC showed a multiphasic pattern with 2–3 points of inflection (Figs. 3, 4). The EFPs were averaged and points of inflection were detected using a semi-automatic peak detection procedure and visual validation using a custom matlab script (that we make available upon requests). For peak detection, we first normalized the LFP responses by subtracting the mean pre-stimulation baseline activity and dividing by the baselines' standard deviation. We then used detected peaks and troughs as change points that were larger than or smaller than three standard deviations from baseline and which were not preceded or followed by other change points exceeding this threshold within 4 msec (the results did not change when using 5 or 10 ms). This procedure ensures that peaks were not mere deflections of noisy LFPs but were stimulation-triggered phenomena. We visually validated these automatically generated peaks in a second step, for which we also plotted the first and second derivative of the LFP signals following stimulation as additional confirmation of the precise sample time of peaks. Peak detection was performed 'blinded', i.e., without knowledge of the recording location of the recorded channel. For each peak, we extracted the amplitude and latency of the components following the procedure and terminology in Wallace et al., (2014).

To statistically test the effect of the area, the anterior–posterior distance relative to the interaural line and the different number of pulses on the latencies (Fig. 7), we carried

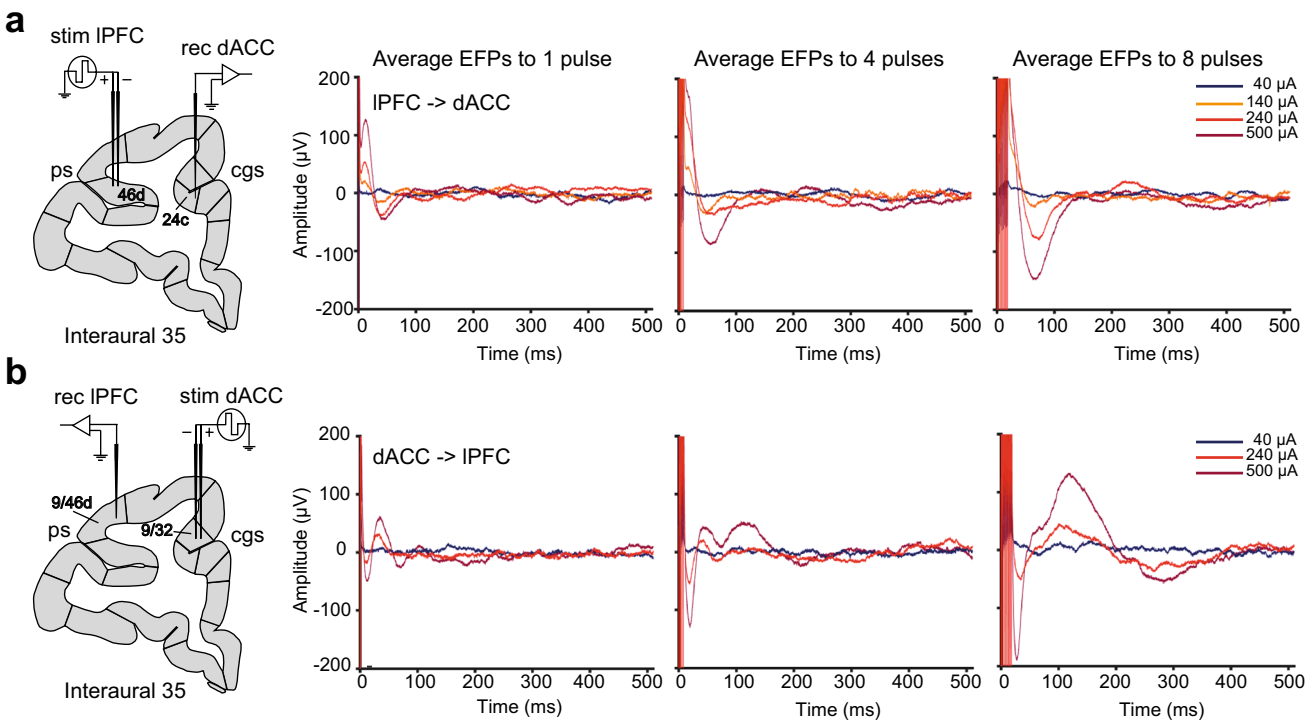

Fig. 3 EFP amplitudes for different stimulation intensities and number of stimulation pulses. **a** Left, example experimental setup for lPFC stimulation and dACC recording. Right, EFP averages over 40 trials of stimulation recorded in dACC. The amplitude of evoked potentials increased from 1 to 8 pulses and 140 to 500 µA stimulation intensity. Note that no EFPs were elicited with 40 µA stimulation current. **b** Same description as in **c**, but for examples of EFPs recorded in lPFC when dACC was stimulated

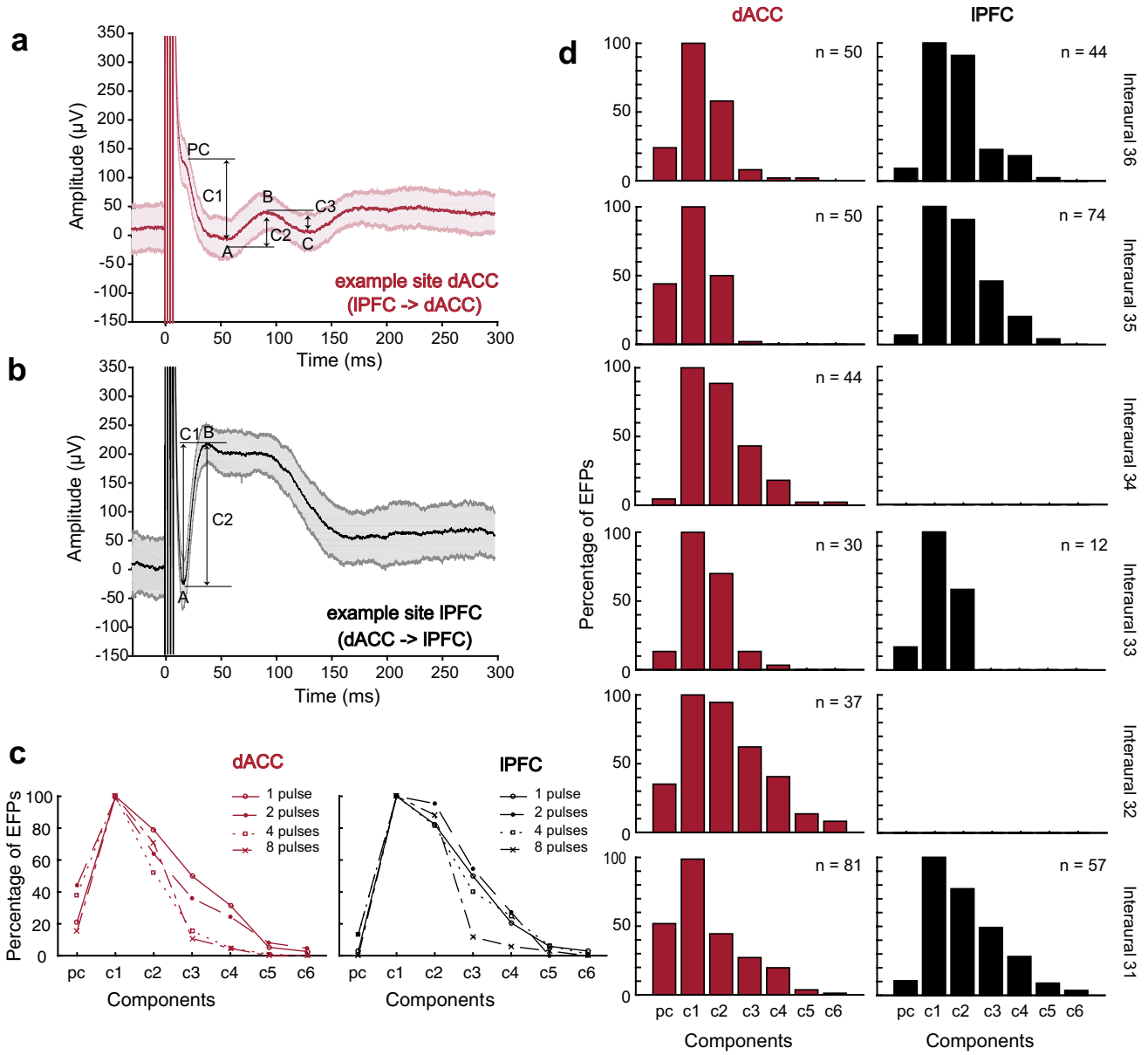

Fig. 4 Typical averaged EFPs elicited in dACC (**a**) and lPFC (**b**). Vertical lines correspond to the stimulation artifacts. Shaded error bars represent the variability of the averaged EFPs over 40 trials (mean ± SEM). Stimulation parameters: 4 pulses burst, 500 μA. Letters mark the distinct points of inflection and arrows show how these were converted into components PC and C1–C3 (Wallace et al. 2014). **c** Percentage of EFPs (*y*-axis) showing the individual components (*x*-axis) when stimulated with different number of pulses. **d** Histograms showing the distribution of dACC and lPFC waveform components across the different interaural coordinates. EFPs recorded during mapping experiments are not included. The lPFC circuits showed significantly more periods (C2–C4 components) of the evoked field potential (see text for details). We could not find evoked responses in lPFC for coordinates 34 and 32, and found very sparse responses in coordinate 33. Note the multiphasic property of the EFPs

out N-way ANOVAs. The dependent variable was the peak latency of the first peak component (C1) of the EFPs and the independent factors were the area (dACC and lPFC), the interaural coordinates (36–31) and the number of pulses (1, 2, 4, and 8). In this analysis, post hoc contrasts using the Tukey–Kramer test were carried out for pair-wise comparison between the interaural coordinates and number of pulses, where appropriate. In a similar way, for assessing the effect of the anterior–posterior distance relative to the interaural line on the number of elicited EFPs (Fig. 4d), we used a one-way ANOVA. The dependent variable was the number of elicited EFPs and the factor was the interaural group (36, 35, 31 versus 34, 33, 32). In this analysis, post hoc contrasts using the Tukey–Kramer test were carried out to perform

pair-wise comparisons between the interaural coordinates group.

Kruskal–Wallis Tests were conducted to examine the differences on the average cycle durations according to the brain region (dACC, lPFC) (Fig. 5). We reported the p value for a test of the null hypothesis that the data in each categorical group (brain region) come from the same distribution. The alternative hypothesis is that not all groups come from the same distribution. When testing individual cycle durations for dACC versus lPFC, Wilcoxon rank-sum tests were performed. All significant difference level was set at $p < 0.05$.

Histology

At the end of the experiments, we confirmed the recording and stimulation sites in the first monkey by marking micrelectrode tracks with a fluorescent dye (DiCarlo et al. 1996). Microelectrodes were coated with a commercial dye (DiI, 50 mg/ml, Sigma-Aldrich) before penetrating them at specific experimental stereotaxic coordinates in lPFC and dACC. Coating the microelectrodes with DiI allows each penetration to be located because it has a unique fluorescent absorption/emission signatures (550/565 nm peak) observable using a fluorescent microscope (Fig. 1b–e). The technique involves no treatment of the tissue other than standard perfusion and sectioning. The monkey was deeply anesthetized and perfused through the heart with saline followed by 3% formaldehyde. Each microelectrode penetration was marked on the surface map of the brain area. The brain was removed and kept in 3% formaldehyde and cryo-protected with 20% sucrose solution. Blocks of the brain were removed from the right hemisphere and sectioned into 50 µm-thick coronal slices parallel to the electrode tracks. Slices were collected into cold phosphate buffer and mounted on gelatin-coated slides. A fluorescent microscope was used to confirm the trajectories of the microelectrodes. Next, the slices were stained with cresyl violet to obtain anatomical information and stored.

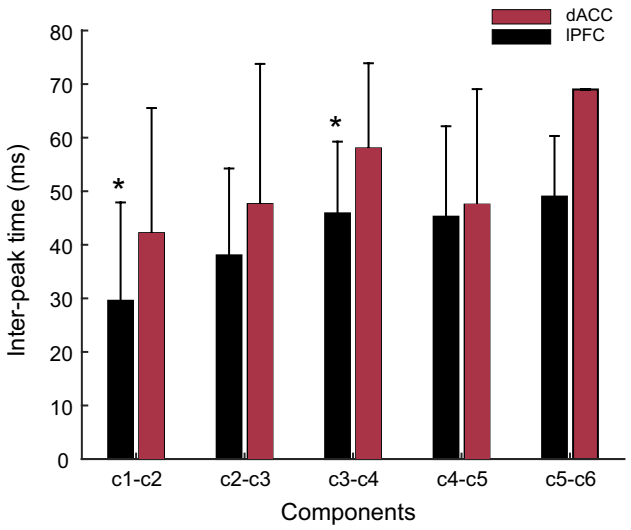

Fig. 5 Average duration ± s.e.m between subsequent components of the multiphasic evoked responses in dACC and lPFC. We only had one dACC datapoint for the C5 → C6 period. *$p < 0.05$ (Wilcoxon rank-sum test, see text for full details)

Results

We combined electrical microstimulation in one brain area and multi-electrode recordings in the other brain area to investigate the nature and pattern of neural activity that effectively links the dACC and lPFC in two rhesus macaque monkeys. We will first report the EFP responses using different microstimulation protocols, and then report the temporal profile, distance and depth dependence of stimulation triggered EFPs in dACC and lPFC.

Stimulation-triggered evoked field potentials and their temporal response profile

A total of 243 pairs of stimulating and recording sites were tested in two monkeys (Monkey $S = 93$; Monkey $H = 150$, Fig. 1a) under several stimulation protocols combining different number of pulses (1, 2, 4, and 8) and stimulation intensities (40, 140, 240, and 500 µA). Across all sessions 812 electrical stimulation protocols were tested. 479 protocols were measured to characterize the typical evoked responses using all pulse types, while 333 protocols were measured to map the depth profile of the microstimulation effects using only the effective protocols eliciting reliable evoked fields.

At the beginning of each experiment we mapped the EFP amplitudes for different stimulation intensities and number of stimulation pulses (Fig. 3). Both in dACC and lPFC, EFPs were reliably evoked at a minimum stimulation intensity of 140 µA with an increased proportion of sites showing evoked fields with larger amplitudes (Fig. 2b). Following the stimulation artifact, the majority of EFPs were multiphasic, showing up to six points of inflection (for example sites from the dACC and lPFC, see Fig. 4a, b). The first point was a low-amplitude negative deflection, similar to a component that previous studies considered to be a putative presynaptic component (PC) because it was unaffected by glutamate blockade (Wallace et al. 2014). The PC was not always present and the probability of its occurrence was higher in EFPs recorded in dACC after lPFC stimulation [χ^2 (1) = 24.61, $p < 0.0001$], following bursts of 2 and 4 pulses (Fig. 4c, d). The majority of EFPs had an initial trough (*labeled 'A'* in Fig. 4a, b), followed by a peak ('B') and a trough ('C').

The average duration between evoked components ranged from 30 to 60 ms, indicative of $a \sim 16$–30 Hz beta frequency band resonance (Fig. 5). The duration of these resonance cycles was shortest for initial C1 → C2 evoked components than for later components in both dACC and lPFC (Fig. 5). A Kruskal–Wallis Test was used to test the differences on the average cycle durations according to the brain region. The average cycle durations were longer in dACC than in lPFC [$H(1) = 20.88$, $p < 0.0001$], with a mean rank of 44 ms for dACC and 29 ms for lPFC. When testing individual cycle durations for dACC versus lPFC, we found significantly different durations for C1 → C2 (Wilcoxon rank-sum, 1683, $p < 0.0001$), and C3 → C4 (Wilcoxon rank-sum, 552, $p < 0.005$). There was no apparent difference in dACC versus lPFC for the durations of C2 → C3 (Wilcoxon rank-sum, 1717, $p = 0.0992$), and C4 → C5 (Wilcoxon rank-sum, 26, $p = 0.9657$).

Across stimulation-recording pairs, we found differences in the number of components as a function of the number of pulses delivered during the stimulation (Fig. 4c). In general, the number of components for a given EFP decreased when using more stimulation pulses. In both areas a large proportion of EFPs following 8 pulses of burst stimulation had only 2 components (C1 and C2). However, the EFPs following single or double pulses showed a more complex waveform with 4 or more components.

Anatomical distribution of stimulation-triggered field potentials

We next quantified the distribution of the PC and C1–C6 components at different interaural (anterior-to-posterior) coordinates (Fig. 4d). In lPFC, the number of elicited EFPs was significantly different for the more anterior (interaural 36 and 35) and the most posterior (interaural 31) coordinates compared with interaural 32, 33, and 34 [$F(1,5) = 32.28$, $p < 0.005$]. Post hoc comparisons using the Tukey–Kramer test indicated that the mean score for interaural 36, 35, and 31 was significantly higher ($M = 58.33$, SD = 15.04) than the mean score for interaural 34, 33, and 32 ($M = 4$, SD = 6.92). In contrast, for dACC sites the amount of elicited EFPs recorded was similar across all the interaural coordinates explored, although a slightly higher number of evoked fields were found at interaural coordinates 35, 36, and 31, but these did not reach statistical significance [$F(1,5) = 4.42$, $p = 0.1033$]. For these locations, there were differences in the percentage of EFPs with PC, with higher percentage of PC's in dACC [$\chi^2(1) = 42.38$, $p < 0.0001$]. The percentage of elicited C1 components in both areas was similar, but there were differences in the percentage of EFPs that showed C2–C4, with larger percentages for lPFC (C2: $\chi^2(1) = 14.70$, $p < 0.0001$; C3: $\chi^2(1) = 32.11$, $p < 0.0001$; C4: $\chi^2(1) = 18.98$, $p < 0.0001$]. Importantly, no EFPs were elicited in lPFC when stimulation in dACC was delivered at interaural coordinates 34 or 32, indicating that the anatomical connections between dACC and lPFC are not completely bidirectional at this point, at least with the explored stimulation-recording sites (Fig. 1). In fact, the number of EFPs recorded in both dACC and lPFC areas at interaural 33 was the lowest, compared with the other explored coordinates. For the lPFC, few EFPs were activated meaning a weaker connection in the direction of dACC-to-lPFC.

The overall relationship of stimulation intensity, number of stimulation pulses and EFP amplitude is shown in Fig. 6. For single- and dual-stimulation pulses there was a

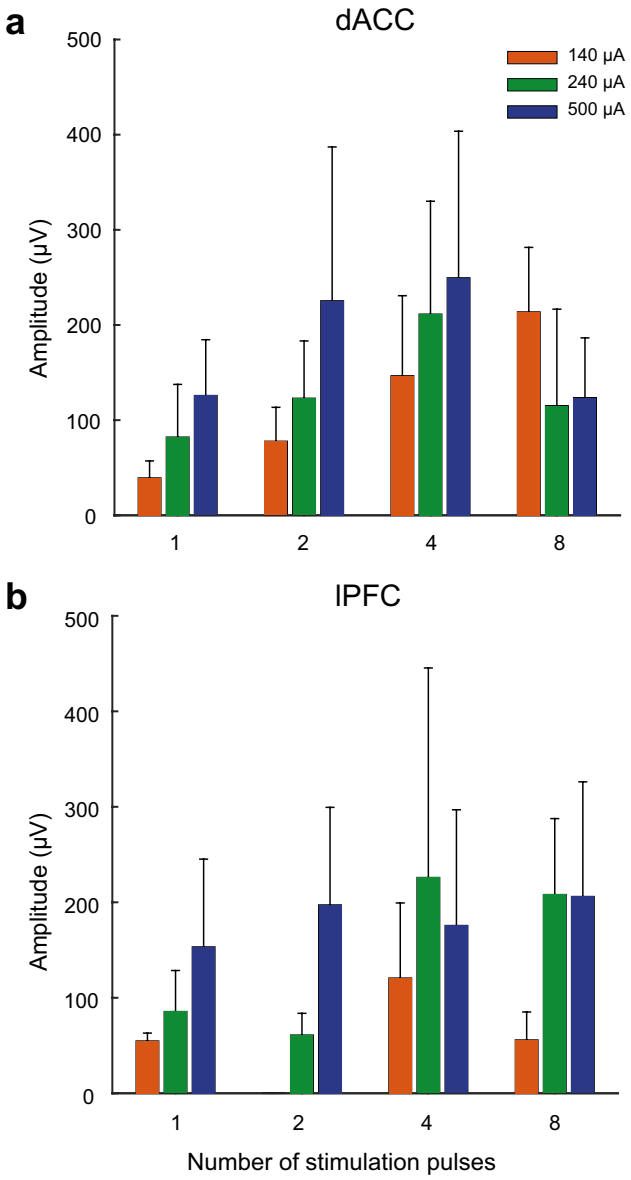

Fig. 6 Relationship between stimulation intensity, number of pulses and EFP amplitude. **a** dACC EFP amplitude modulation. **b** lPFC EFP amplitude modulation. Each bar represents mean ± s.e.m of the C1

systematic increase in the mean EFP amplitude with increasing pulse strength in both the dACC (Fig. 6a) and lPFC (Fig. 6b). Stimulating with ≥ 3 stimulation pulses resulted in a more variable relationship between stimulation intensity to EFP amplitudes, with reduced EFP amplitudes observed for most stimulation protocols involving 8 pulses.

Latencies of stimulation-triggered evoked field potentials

The median peak latency of the C1 of the EFPs varied across the interaural coordinates and with increasing number of stimulation pulses (Fig. 7). We tested the effect of the area, the anterior–posterior distance relative to the interaural line and the number of stimulation pulses on the latencies performing an N-way ANOVA. Latencies for C1 were shortest when dACC was stimulated and lPFC was recorded from the most anterior (interaural 36 and 35) and posterior (interaural 31) coordinates: interaural 36 [F (1,68) = 212.07, $p < 0.0001$], interaural 35 [F (1,82) = 687.72, $p < 0.0001$], interaural 33 [F (1,29) = 0.00003, $p = 0.3348$] and interaural 31 [F (1,105) = 15.96, $p = 0.0001$]. Also, the difference between these latency values increased with the number of pulses for these specific coordinates. Single pulse (lPFC: 10–14 ms; dACC: 28–38 ms) [F (1,36) = 60.82, $p = 0$], 2 pulse bursts (lPFC: 10–20 ms; dACC: 33–45 ms) [F (1,63) = 15.55, $p = 0.0002$], four-pulse bursts (lPFC: 18–20 ms; dACC: 45–57 ms) [F (1,134) = 93.98, $p < 0.0001$], and eight-pulse bursts (lPFC: 24–59 ms; dACC: 70–79 ms) [F (1,51) = 17.9, $p = 0.0001$]. Interaural 33 was exceptional in that latencies were long and similar for both areas. The asymmetries in latencies found for the most anterior and posterior coordinates could indicate differential synaptic connectivity profiles in both directions.

Effects of variation in stimulation depths on evoked field potentials

We next explored whether long-distance microstimulation effects varied across laminar depth and were restricted to connections originating in gray matter. For this purpose, we mapped effective connectivity between dACC and lPFC at different depths across the cortex using stimulation protocols (2 or 4-pulse bursts at 500 µA supra-threshold intensity) which elicited evoked fields for most connections in the previous experiments (Fig. 2b). Figure 8 shows the effects of changing the depths of stimulation microelectrodes on the EFPs in different dACC and lFPC subfields. During a representative mapping experiment shown in Fig. 8a (data from Monkey S), the recording microelectrodes remained at the same location in dACC (area 24c) while the stimulation microelectrodes were lowered into lPFC area 46d over a range of ~ 2 mm until we observed a clear drop in the long-range-evoked field amplitude (Fig. 8a, red arrow represents the direction of the mapping). Across this depth range microstimulation had initially no effect on the dACC-recording sites and then showed an 'M'-like laminar-effective connectivity profile for both dACC-recording sites with

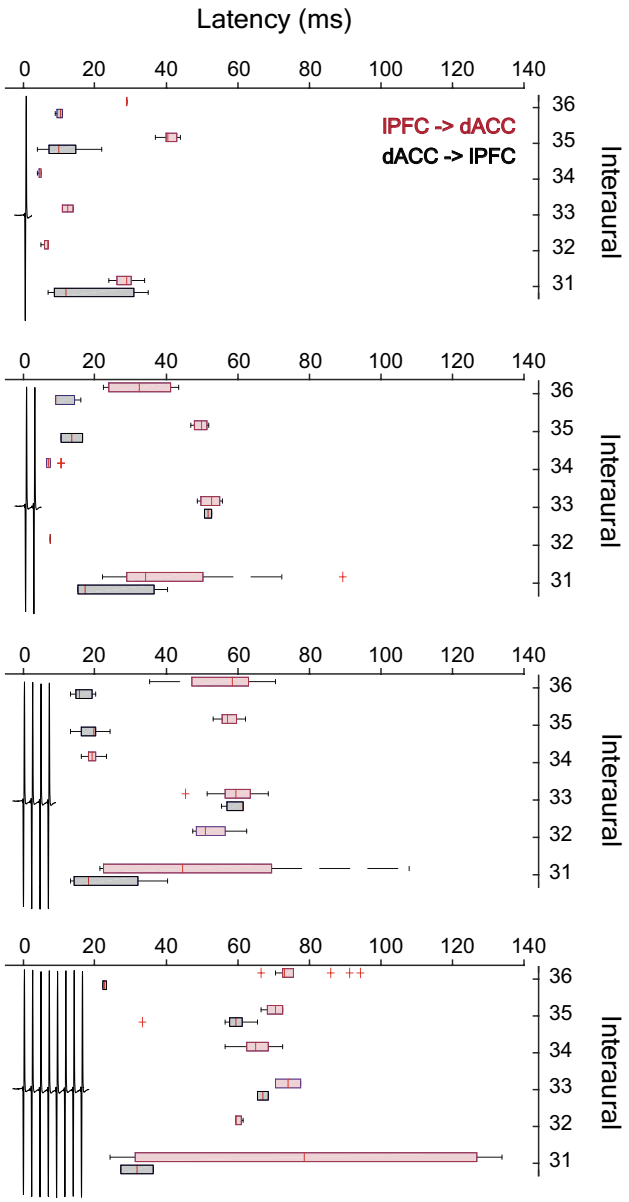

Fig. 7 Latencies of EFPs at different interaural coordinates for 1–8 stimulation pulses. Shown are the box plots of the C1 component of the EFPs in the dACC (dark red squares) and in the lPFC (black squares) at the different interaural coordinates (y-axis). The left and right of each box are the 25th and 75th percentiles of the latencies, respectively. The vertical red line inside the box is the median of the latencies. The whiskers are lines extending left and right of each box and show the extent of the minimum and maximum latency values. Observations beyond the whisker length are displayed as outliers with a red + sign. The number of pulses is represented by the stimulation artifacts plotted at the actual trial time

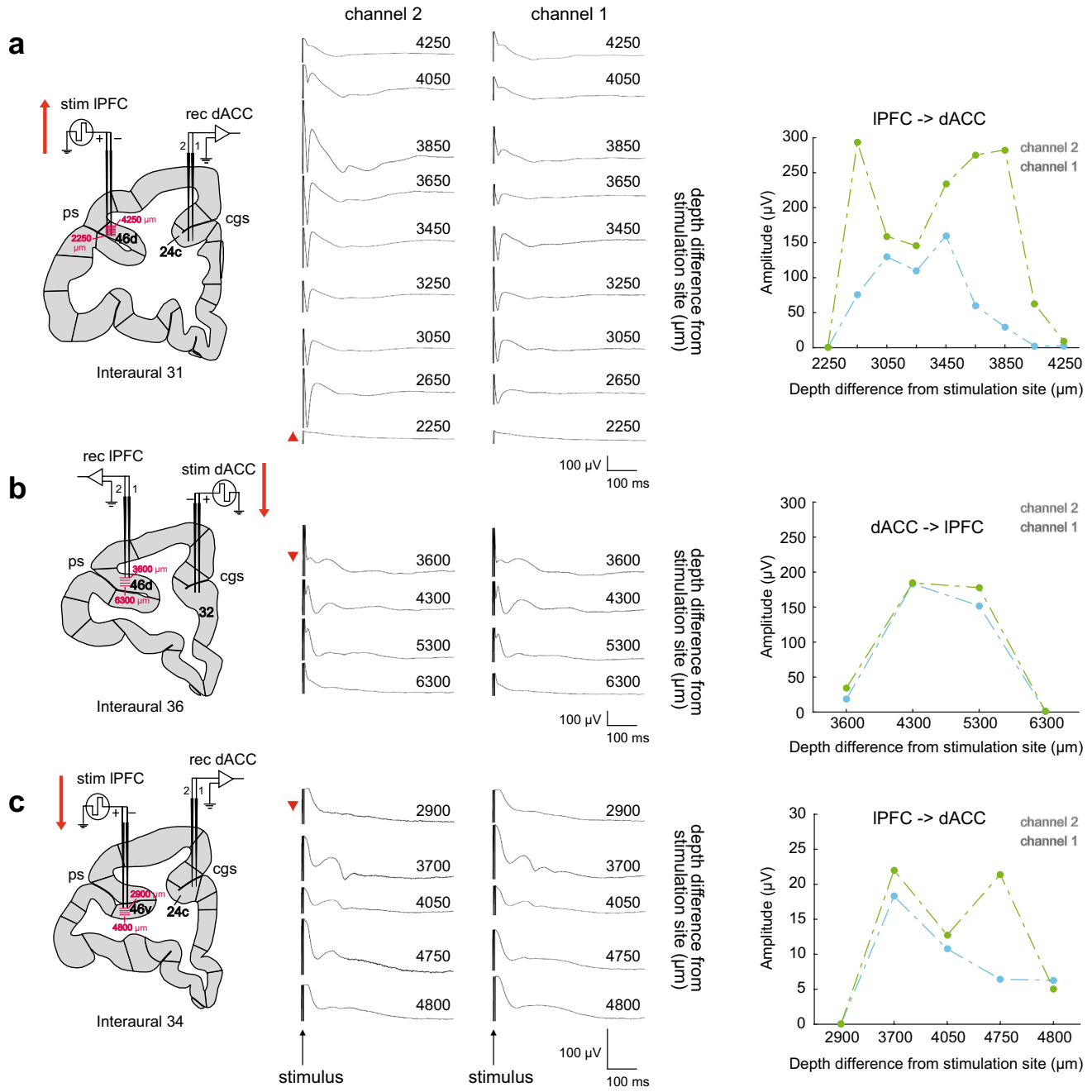

Fig. 8 Representative inter-laminar mapping of the long-distance microstimulation effects between dACC and lPFC areas. **a** Effects of changing the depth of the stimulation microelectrodes. Each EFP was recorded at the same depth in right area 24c (channels 1 and 2), with the position of the stimulation electrodes in lPFC area 46d changing in the ventrodorsal direction (red arrow represents the direction of the mapping). The red triangle to the left of a specific recording trace depicts the starting mapping location and its direction. The red horizontal lines in the coronal slice plots (left panel) represent the approximate levels of the different stimulation sites. Numbers above each recording trace denote the depth difference value of the recording from the stimulation site in µm (depth difference = | recording depth − stimulation depth |). Stimulation parameters: 2 pulses burst, 500 µA. Plot on the right shows the layer-specific EFP amplitude modulation for the C1 and the extent of the microstimulation effects. **b** Effects on lPFC area 46d EFPs of changing the depth of the stimulation electrodes in area 32. Stimulation parameters: 4-pulses burst, 500 µA. **c** Effects on area 24c EFPs of changing the depth of the stimulation electrodes in area 46v. Stimulation parameters: 4-pulses burst, 500 µA. *ps* principal sulcus, *cgs* cingulate sulcus

increasing depth of the stimulation site. The dip in the middle of the depth profile spanned $a \sim 600$ µm window where the evoked field amplitudes were below the peak amplitudes at more superficial or deeper recording sites. In other mapping experiments with varying stimulation depth in the dACC and recordings in dorsal lPFC (Fig. 8b) or with varying stimulation depth in the ventral bank of the principle sulcus of the lPFC and recordings in dACC, we observed bell-shaped depth profiles (Fig. 8b), or mixtures of bell-shaped and M-shaped (Fig. 8c) depth profiles spanning ~ 1.5 mm cortical distance in which stimulation triggered evoked fields. These findings indicate that systematic depth variations of effective connectivity might exist, and that overall, effective microstimulation effects at the intensities tested are restricted to cortical gray matter.

Discussion

We found a microelectrical stimulation protocol for mapping the strength, latency and temporal patterning of effective connectivity between dACC and lPFC in the awake nonhuman primate. Effective synaptic connectivity was reliably evoked with 140 µA pulses in half of all connections in both directions, increasing systematically with increasing amplitudes up to ~ 500 µA. Whether two sites within the dACC and lPFC were connected depended on the precise anterior-to-posterior locations in a patchy way with no apparent linear gradient. Despite this heterogeneity, we observed reliable directional asymmetries of the dACC–lPFC connectivity. dACC stimulation triggered faster latency-evoked components in the lPFC and resulted, more likely, in a multiphasic response pattern with 2–4 inflection points when compared to stimulating the same connection from the lPFC and measuring the evoked component in the dACC. These findings provide to the best of our knowledge the first delineation of effective connectivity among dACC and lPFC in the awake monkey brain, pointing to anatomically patchy connectivity that shows an asymmetric temporal profile. We speculate that these effective connectivity findings reflect patchy and asymmetric synaptic connectivity at the anatomical level, and might translate into differences in neuronal information flow during functional states that depend on dACC–lPFC contributions.

Eliciting long-range connectivity with single and dual electrical pulses

Our study identified a bipolar, biphasic, constant-current electrical stimulation protocol that reliably evokes long-range LFP responses for most dACC-to-lPFC and lPFC-to-dACC long-range connections consistent with known functional connectivity (Hutchison et al. 2012). This protocol deviates significantly from previous studies reporting long-range electrical stimulation effects on blood flow responses using functional magnetic resonance imaging (fMRI) (Matsui et al. 2011; Tolias et al. 2005; Ekstrom et al. 2008; Moeller et al. 2008; Field et al. 2008; Premereur et al. 2015; Logothetis et al. 2012). When testing protocols that are similar to those used in fMRI studies such as, e.g., using trains of biphasic pulses (25–50 pulses) at 100 Hz with current intensities ranging from 20 to 240 µA, we failed to observe reliable evoked fields. In our setting, it was sufficient to use single and dual pulse stimulation to trigger-evoked fields at 140–500 µA.

Long-distance activation is multiphasic and could indicate circuit-specific resonance

We found that a main characteristic of long-range-evoked responses was a multiphasic temporal response pattern. For more than half of all connections, microstimulation triggered a dynamic, multiphasic response with two or more peaks. These multiphasic EFPs displayed a recurrent negative–positive pattern of several cycles with decreasing amplitude suggestive of a recurrent excitatory loop (Wallace et al. 2014). This could indicate that neurons closer to the recording site in the activated long-distance area, either dACC or lPFC, respond more effectively to inputs of a particular low-frequency range which is reflected in the shape of the EFP. We interpret this as resonance phenomenon that could help to understand the underlying mechanisms of synaptic integration (Buzsaki et al. 2012; Hutcheon and Yarom 2000). Consistent with this interpretation, modeling studies suggest that resonance, as measured in LFP signals, is well retained close to the cell somata when the synaptic inputs are concentrated at the apical dendrites (Ness et al. 2016). Resonance phenomena are more difficult to measure when inputs are distributed more uniformly across apical and basal dendritic trees (Ness et al. 2016). We believe that the widespread rhythmic resonance effects we observed even following single, non-rhythmic input pulses makes it likely that a similar resonance phenomenon might be effective during intrinsic information processing. The functional consequences of such intrinsic resonance effects have been discussed in detail in the framework of neuronal '*communication though resonance*' (CTR) (Hahn et al. 2014). CTR is built on the observation that in local circuits with asynchronous-irregular firing activity without apparent ongoing oscillations in the LFP activity, already subtle resonance can lead to the amplification of input over successive cycles within the resonant frequency (Hahn et al. 2014). According to these computational insights the observed beta band resonance in both dACC and lPFC circuits, could reflect an intrinsic mechanism for enhanced recurrent communication

between both areas triggered by task demands or internal state changes.

Relation of evoked-field latencies and temporal pattern to neuroanatomical differences between dACC and lPFC

Important contributions to the resonance of a circuit are the type and the time constants of inhibition (Womelsdorf, Valiante et al. 2014). Our finding that the lPFC circuits showed significantly more periods (C2–C4 components) of the evoked field potential might therefore relate to differences in inhibition in the dACC and lPFC that have been particularly well documented (Medalla et al. 2009, 2017; Dombrowski et al. 2001). In particular, a series of neuroanatomical studies have revealed systematic differences in multiple neuroanatomical and physiological markers of inhibition between lateral lPFC (area 46), and dACC (including the rostral area 32). Among these differences are at least four that influence latencies and temporal patterning of responses to inputs and hence are consistent with the observed electrical stimulation triggered dACC/lPFC asymmetries.

As a first well-documented anatomical difference, axonal projections from agranular and dysgranular dACC to eulaminate (granular) lPFC cortex originate from deeper layers (layers V and VI) and terminate in supragranular layers I, II and IIIa (Barbas and Pandya 1989; Barbas 2015; Garcia-Cabezas et al. 2017). In contrast, connections in the reverse direction from lPFC → dACC have an opposite gradient originating largely from upper and middle layers II and III and projecting to middle and deeper layer IIIb, V and VI (Barbas and Rempel-Clower 1997; Medalla and Barbas 2010; Barbas et al. 2005). The laminar-specific connectivity suggests that microstimulation in ACC will affect predominantly superficial neurons in lPFC, while lPFC stimulation will affect predominantly neurons in middle-deep ACC layers. This layer specificity of inputs to ACC versus lPFC could relate to the asymmetries in latencies and temporal patterning of effective connectivity in the light of studies reporting differently strong rhythmic activities in the alpha/beta bands across layers in frontal cortex (Bastos et al. 2018; Ninomiya et al. 2015).

A second prominent anatomical asymmetry is the composition and density of inhibitory synapses and interneurons between ACC and lPFC (Dombrowski et al. 2001; Medalla et al. 2017; Garcia-Cabezas et al. 2017). In the macaque, slower acting calbindin (CB+) expressing interneurons are more numerous in ACC than in PFC, while parvalbumin expressing (PV+) inhibitory interneurons are more than twice as numerous in lPFC than in ACC (Dombrowski et al. 2001). Moreover, a recent study found additional differences, showing that macaque ACC pyramidal cells (compared to PFC cells) received three times more synapses from cholecystokinin expressing (CCK+) interneurons targeting the perisomatic region where they can exert control over AP generation (Medalla et al.., 2017). CCK+ interneurons express more ubiquitously the alpha 2 subunit and have a slower decay kinetics than fast spiking parvalbumin expressing (PV+) interneurons (Nyiri et al. 2001; Klausberger et al. 2002). Functionally CCK+ interneurons are implicated to impose an inhibitory tone on a pyramidal cell network as opposed to PV+ fast spiking interneurons linked to fast rhythmic synchronization of pyramidal cells (Klausberger et al. 2005; Womelsdorf et al. 2014a, b). Intriguingly, we found that the latency of evoked responses within the dACC (with lPFC→ dACC stimulation) was on average slower than in LPFC (with dACC → lPFC stimulation), which is consistent with an enhanced inhibitory tone in dACC versus lPFC that needs to be overcome to respond to incoming current. This conclusion is also supported by direct evidence for an enhanced inhibitory tone in macaque anterior ACC versus lPFC slices (Medalla et al. 2017). These differences give rise to an overall lower excitation-inhibition ratio in ACC than PFC due to larger number of inhibitory postsynaptic potentials (IPSCs) and overall more inhibitory spines (Medalla et al. 2017).

A third physiological difference with direct functional consequences of the different types and degrees of inhibition in ACC and PFC have been directly tested in the slice where IPSCs in dACC show slower decay time constant compared to lPFC (Fig. 8 in Medalla et al. 2017). The consequences of slower inhibitory decay times in computational models is a slowed frequency of rhythmic oscillatory activity in the population of interconnected pyramidal cells (discussed in Medalla et al. 2017; see, Gloveli et al. 2005; Tort et al. 2007; Kopell et al. 2010). These in vitro and modeling results thus provide a parsimonious explanation of our finding of a longer cycle duration of evoked potentials in dACC compared to lPFC (Fig. 5). In summary, the differences in the profiles of inhibition in lPFC and dACC likely underlie the different temporal patterning of long-range-triggered evoked responses that we observed following electrical microstimulation.

A fourth anatomical difference is the overall lower cell density in dACC compared with the lPFC superficial layers II and III (Dombrowski et al. 2001; Gabbott and Bacon 1996). A larger cell density will allow a faster spread of input current in the receiving circuit (McIntyre and Grill 2000), and hence could also underlie faster evoked responses in the lPFC than in dACC. Although we cannot eliminate the possibility of more complex dendritic integration effect given that basal dendritic fields are larger in ACC (Elston et al. 2005, 2011), or more complex synaptic pathways between the stimulating and recording sites, an overall difference in cell density complements the differences in inhibition

described above in determining the latencies and temporal patterning of the evoked responses to external inputs.

Effective connectivity shows discontinuities similar to anatomical connectivity

By varying the anterior-to-posterior location of stimulation and recording sites we were able to discern that the strength and latencies of electrically evoked field components could vary abruptly from one anterior-to-posterior section to the next section 1 mm away (Figs. 4, 6). Such discontinuities in the strength of effective synaptic connectivity are consistent with a rich literature documenting patchiness and discontinuities of the underlying anatomical connectivity of the medial and lateral prefrontal cortex including dACC and lPFC (Goldman and Nauta 1977; Barbas and Pandya 1989; Cavada et al. 2000). Previous anatomical tracing studies have shown that both brain regions we recorded and stimulated, rostral dACC and the ventral and dorsal bank of the principal sulcus (lPFC), are reciprocally connected over a wide anterior-to-posterior range (Arikuni et al. 1994; Lu et al. 1994). However, visually inspecting the density and distribution of cells in the lPFC that were retrogradely labeled by large tracer injections in the dACC reveals dramatic variations from one coronal slice to the next (Arikuni et al. 1994; Barbas and Pandya 1989; Cavada et al. 2000). While cells can show labeling over several coronal slices, occasionally a slice shows reduced labeling or lacks labeling altogether. These anatomical discontinuities could well underlie the abrupt variations in latencies we observed between interaural 31 mm and 32 mm or between interaural 34 mm and 35 mm (Fig. 7, upper panel).

A similar anatomical origin might also underlie the two different depth profiles of effective connectivity we observed. We found that long-range evoked fields showed bell-shaped or 'M'-shaped profiles when lowering the stimulation electrodes through the layers inside the gray matter (Fig. 8). These two types of patterns can likewise be seen in the density profiles of labeled projection cells traced with retrograde tracers between dACC and lPFC. For example, Arikuni et al. (1994) presented a case with tracer injection in the rostral dACC that caused patchy, retrograde labeling of cells in the ventral bank of the principal sulcus (lPFC) in the form of a superficial cluster and a deep layer cluster similar to an M-pattern (e.g., Fig. 2, Sects. 14 and 16 in Arikuni et al. 1994). Similar patterns with two layers of retrogradely labeled cells are evident in other studies (e.g., Fig. 9c, Sect. 2 in Morecraft et al. 2012), suggesting that cortico-cortical connections between dACC and lPFC proceed through two separate routes in upper and lower layers. In addition to the 'two striped', or 'M-shaped' pattern in anatomically tracing, several slices show a more homogeneous labeling with only a single cluster of cells across laminae with the highest density of connections in the center of the cluster, reminiscent of a bell-shaped profile. These anatomical studies thus provide connectivity profiles similar to those that we observed in profiles of effective connectivity in the awake monkey.

Conclusion

In summary, our study revealed systematic asymmetries in the latencies and temporal patterning of dACC–lPFC effective connectivity, suggesting a more rapid and more temporally patterning of dACC → lPFC effects than lPFC → dACC effects. These results identified a parameter range for the intensity and number of biphasic cathode-first-anode-second pulse types that reliably evoke field potential flow in the receiving brain circuit. This overall pattern of effective connectivity was complemented by anisotropies of stimulation effects across layers, and by patchy stimulation effects that showed stronger and weaker connectivity at anatomical sites spaced as little as 1 mm away from each other. We believe that the findings of systematic asymmetries in effective connectivity might be reflected in asymmetries of functional connectivity and could originate from complex variations of synaptic connectivity between the dACC and lPFC. Future studies could clarify this suggestion by combining measuring effective and functional connectivity protocols in the same experimental set up and applying synaptic dual tracers for antero- and retrograde labeling of inter-area connections. Such a multi-method approach could resolve how structural and functional connectivity relate to each other to subserve the network-level functions that co-activation of dACC and lPFC realizes during goal-directed behavior.

Acknowledgements This work was supported by a grant from the Canadian Institutes of Health Research (T.W.). CIHR Grant MOP_102482. The funders had no role in study design, data collection and analysis, the decision to publish, or the preparation of this manuscript. The authors would like to thank Hongying Wang for technical support.

Compliance with ethical standards

Conflict of interest The authors declare that they have no conflict of interest.

Ethical approval All animal care and experimental procedures performed in this study have been approved by the local ethics committee, the York University Council on Animal Care, were in accordance with the Canadian Council on Animal Care guidelines, and are in agreement with the 1964 Helsinki Declaration and its later amendments.

References

Alexander WH, Brown JW (2011) Medial prefrontal cortex as an action-outcome predictor. Nat Neurosci 14:1338–1344

Arikuni T, Sako H, Murata A (1994) Ipsilateral connections of the anterior cingulate cortex with the frontal and medial temporal cortices in the macaque monkey. Neurosci Res 21:19–39

Barbas H (2015) General cortical and special prefrontal connections: principles from structure to function. Annu Rev Neurosci 38:269–289

Barbas H, Pandya DN (1989) Architecture and intrinsic connections of the prefrontal cortex in the rhesus monkey. J Comp Neurol 286:353–375

Barbas H, Rempel-Clower N (1997) Cortical structure predicts the pattern of corticocortical connections. Cereb Cortex 7:635–646

Barbas H, Hilgetag CC, Saha S, Dermon CR, Suski JL (2005) Parallel organization of contralateral and ipsilateral prefrontal cortical projections in the rhesus monkey. BMC Neurosci 6:32

Bastos AM, Loonis R, Kornblith S, Lundqvist M, Miller EK (2018) Laminar recordings in frontal cortex suggest distinct layers for maintenance and control of working memory. Proc Natl Acad Sci USA 115:1117–1122

Buzsaki G, Anastassiou CA, Koch C (2012) The origin of extracellular fields and currents—EEG, ECoG, LFP and spikes. Nat Rev Neurosci 13:407–420

Cavada C, Company T, Tejedor J, Cruz-Rizzolo RJ, Reinoso-Suarez F (2000) The anatomical connections of the macaque monkey orbitofrontal cortex. A review. Cereb Cortex 10:220–242

DiCarlo JJ, Lane JW, Hsiao SS, Johnson KO (1996) Marking microelectrode penetrations with fluorescent dyes. J Neurosci Methods 64:75–81

Dombrowski SM, Hilgetag CC, Barbas H (2001) Quantitative architecture distinguishes prefrontal cortical systems in the rhesus monkey. Cereb Cortex 11:975–988

Ekstrom LB, Roelfsema PR, Arsenault JT, Bonmassar G, Vanduffel W (2008) Bottom-up dependent gating of frontal signals in early visual cortex. Science 321:414–417

Elston GN, Benavides-Piccione R, Defelipe J (2005) A study of pyramidal cell structure in the cingulate cortex of the macaque monkey with comparative notes on inferotemporal and primary visual cortex. Cereb Cortex 15:64–73

Elston GN, Benavides-Piccione R, Elston A, Manger PR, Defelipe J (2011) Pyramidal cells in prefrontal cortex of primates: marked differences in neuronal structure among species. Front Neuroanat 5:2

Field CB, Johnston K, Gati JS, Menon RS, Everling S (2008) Connectivity of the primate superior colliculus mapped by concurrent microstimulation and event-related fMRI. PLoS One 3:e3928

Gabbott PL, Bacon SJ (1996) Local circuit neurons in the medial prefrontal cortex (areas 24a,b,c, 25 and 32) in the monkey: II. Quantitative areal and laminar distributions. J Compar Neurol 364:609–636

Garcia-Cabezas MA, Joyce MKP, John YJ, Zikopoulos B, Barbas H (2017) Mirror trends of plasticity and stability indicators in primate prefrontal cortex. Eur J Neurosci 46:2392–2405

Gloveli T, Dugladze T, Saha S, Monyer H, Heinemann U, Traub RD, Whittington MA, Buhl EH (2005) Differential involvement of oriens/pyramidale interneurones in hippocampal network oscillations in vitro. J Physiol 562:131–147

Goldman PS, Nauta WJ (1977) An intricately patterned prefrontocaudate projection in the rhesus monkey. J Compar Neurol 72:369–386

Hahn G, Bujan AF, Fregnac Y, Aertsen A, Kumar A (2014) Communication through resonance in spiking neuronal networks. PLoS Comput Biol 10:e1003811

Hayden BY, Heilbronner SR, Pearson JM, Platt ML (2011) Surprise signals in anterior cingulate cortex: neuronal encoding of unsigned reward prediction errors driving adjustment in behavior. J Neurosci 31:4178–4187

Hutcheon B, Yarom Y (2000) Resonance, oscillation and the intrinsic frequency preferences for neurons. Trends Neurosci 23:216–222

Hutchison RM, Womelsdorf T, Gati JS, Leung LS, Menon RS, Everling S (2012) Resting-state connectivity identifies distinct functional networks in macaque cingulate cortex. Cereb Cortex 22:1294–1308

Kennerley SW, Walton ME, Behrens TE, Buckley MJ, Rushworth MF (2006) Optimal decision making and the anterior cingulate cortex. Nat Neurosci 9:940–947

Klausberger T, Roberts JD, Somogyi P (2002) Cell type- and input-specific differences in the number and subtypes of synaptic GABA(A) receptors in the hippocampus. J Neurosci 22:2513–2521

Klausberger T, Marton LF, O'Neill J, Huck JH, Dalezios Y, Fuentealba P, Suen WY, Papp E, Kaneko T, Watanabe M et al (2005) Complementary roles of cholecystokinin- and parvalbumin-expressing GABAergic neurons in hippocampal network oscillations. J Neurosci 25:9782–9793

Kopell N, Börgers C, Pervouchine D, Malerba P, Tort AB (2010) Gamma and theta rhythms in biophysical models of hippocampal circuits. In: Cutsuridis V, Graham BF, Cobb S, Vida I (eds) Hippocampal microcircuits: a computational modeller's resource book. Springer, New York, pp 423–457

Logothetis NK, Eschenko O, Murayama Y, Augath M, Steudel T, Evrard HC, Besserve M, Oeltermann A (2012) Hippocampal-cortical interaction during periods of subcortical silence. Nature 491:547–553

Lu MT, Preston JB, Strick PL (1994) Interconnections between the prefrontal cortex and the premotor areas in the frontal lobe. J Comp Neurol 341:375–392

Matsui T, Tamura K, Koyano KW, Takeuchi D, Adachi Y, Osada T, Miyashita Y (2011) Direct comparison of spontaneous functional connectivity and effective connectivity measured by intracortical microstimulation: An fMRI study in macaque monkeys. Cereb Cortex 21:2348–2356

McIntyre CC, Grill WM (2000) Selective microstimulation of central nervous system neurons. Ann Biomed Eng 28:219–233

Medalla M, Barbas H (2009) Synapses with inhibitory neurons differentiate anterior cingulate from dorsolateral prefrontal pathways associated with cognitive control. Neuron 61:609–620

Medalla M, Barbas H (2010) Anterior cingulate synapses in prefrontal areas 10 and 46 suggest differential influence in cognitive control. J Neurosci 30:16068–16081

Medalla M, Gilman JP, Wang JY, Luebke JI (2017) Strength and diversity of inhibitory signaling differentiates primate anterior cingulate from lateral prefrontal cortex. J Neurosci 37:4717–4734

Moeller S, Freiwald WA, Tsao DY (2008) Patches with links: a unified system for processing faces in the macaque temporal lobe. Science 320:1355–1359

Montgomery EB (2010) Deep brain stimulation programming: principles and practice. Oxford University Press, Oxford

Morecraft RJ, Stilwell-Morecraft KS, Cipolloni PB, Ge J, McNeal DW, Pandya DN (2012) Cytoarchitecture and cortical connections of the anterior cingulate and adjacent somatomotor fields in the rhesus monkey. Brain Res Bull 87:457–4997

Ness TV, Remme MWH, Einevoll GT (2016) Active subthreshold dendritic conductances shape the local field potential. J Physiol 594:3809–3825

Ninomiya T, Dougherty K, Godlove DC, Schall JD, Maier A (2015) Microcircuitry of agranular frontal cortex: contrasting laminar connectivity between occipital and frontal areas. J Neurophysiol 113:3242–3255

Nyiri G, Freund TF, Somogyi P (2001) Input-dependent synaptic targeting of alpha(2)-subunit-containing GABA(A) receptors in synapses of hippocampal pyramidal cells of the rat. Eur J Neurosci 13:428–442

Oemisch M, Westendorff S, Everling S, Womelsdorf T (2015) Interareal spike-train correlations of anterior cingulate and dorsal prefrontal cortex during attention shifts. J Neurosci 35:13076–13089

Paxinos G, Huang XF, Petrides M, Toga AW (2008) The rhesus monkey brain in stereotaxic coordinates. Academic Press, London

Premereur E, Van Dromme IC, Romero MC, Vanduffel W, Janssen P (2015) Effective connectivity of depth-structure-selective patches in the lateral bank of the macaque intraparietal sulcus. PLoS Biol 13:e1002072

Rothe M, Quilodran R, Sallet J, Procyk E (2011) Coordination of high gamma activity in anterior cingulate and lateral prefrontal cortical areas during adaptation. J Neurosci 31:11110–11117

Rushworth MF, Noonan MP, Boorman ED, Walton ME, Behrens TE (2011) Frontal cortex and reward-guided learning and decision making. Neuron 70:1054–1069

Shenhav A, Cohen JD, Botvinick MM (2016) Dorsal anterior cingulate cortex and the value of control. Nat Neurosci 19:1286–1291

Tolias AS, Sultan F, Augath M, Oeltermann A, Tehovnik EJ, Schiller PH, Logothetis NK (2005) Mapping cortical activity elicited with electrical microstimulation using fMRI in the macaque. Neuron 48:901–911

Tort AB, Rotstein HG, Dugladze T, Gloveli T, Kopell NJ (2007) On the formation of gamma-coherent cell assemblies by oriens lacunosum-moleculare interneurons in the hippocampus. Proc Natl Acad Sci USA 104:13490–13495

Voloh B, Womelsdorf T (2017) Cell-type specific burst firing interacts with theta and beta activity in prefrontal cortex during attention states. Cereb Cortex 1–17

Voloh B, Valiante TA, Everling S, Womelsdorf T (2015) Theta–gamma coordination between anterior cingulate and prefrontal cortex indexes correct attention shifts. Proc Natl Acad Sci USA 112:8457–8462

Wallace J, Jackson RK, Shotton TL, Munjal I, McQuade R, Gartside SE (2014) Characterization of electrically evoked field potentials in the medial prefrontal cortex and orbitofrontal cortex of the rat: modulation by monoamines. Eur Neuropsychopharmacol 24:321–332

Womelsdorf T, Everling S (2015) Long-range attention networks: circuit motifs underlying endogenously controlled stimulus selection. Trends Neurosci 38:682–700

Womelsdorf T, Ardid S, Everling S, Valiante TA (2014a) Burst firing synchronizes prefrontal and anterior cingulate cortex during attentional control. Curr Biol 24:2613–2621

Womelsdorf T, Valiante TA, Sahin NT, Miller KJ, Tiesinga P (2014b) Dynamic circuit motifs underlying rhythmic gain control, gating and integration. Nat Neurosci 17:1031–1039